All-electron, density-functional-based method for angle-resolved tunneling ionization in the adiabatic regime

Imam S. Wahyutama,[1,*,†] Denawakage D. Jayasinghe,[2,*,‡] François Mauger,[1] Kenneth Lopata,[2,3]
Mette B. Gaarde,[1] and Kenneth J. Schafer[1]
[1]*Department of Physics and Astronomy, Louisiana State University, Baton Rouge, Louisiana 70803, USA*
[2]*Department of Chemistry, Louisiana State University, Baton Rouge, Louisiana 70803, USA*
[3]*Center for Computation and Technology, Louisiana State University, Baton Rouge, Louisiana 70808, USA*

(Received 13 August 2022; accepted 1 November 2022; published 18 November 2022)

We develop and test a method that integrates many-electron weak-field asymptotic theory (ME-WFAT) [O. I. Tolstikhin, L. B. Madsen, and T. Morishita, Phys. Rev. A **89**, 013421 (2014)] in the integral representation (IR) into the density-functional-theory (DFT) framework. In particular, we present modifications of the integral formula in the IR ME-WFAT to incorporate the potential terms unique to DFT. By solving an adiabatic rate equation for the angle-resolved ionization yield in our DFT-based ME-WFAT method, we show that the results are in excellent agreement with those of real-time time-dependent density-functional-theory (TDDFT) simulations for NO, OCS, CH_3Br, and CH_3Cl interacting with one- and two-color laser fields with a fundamental wavelength of 800 nm. This agreement is significant because the WFAT calculations take only a small fraction of the time of full TDDFT calculations. These results suggest that in the wavelength region commonly used in strong-field experiments (800 nm and longer), our DFT-based WFAT treatment can be used to rapidly screen for the ionization properties of a large number of molecules as a function of alignment or orientation between the molecule and the strong field.

DOI: 10.1103/PhysRevA.106.052211

I. INTRODUCTION

Tunnel ionization, wherein an electron driven by an external field moves through the barrier formed by the combination of the molecular and external field potentials, is the ionization process that forms the initial step in many strong-field processes. The study of a range of important physical processes in ultrafast science, such as orientation-dependent strong-field ionization (SFI), high-harmonic generation [1,2], the measurement of time delays in tunnel ionization via the attoclock [3], light-induced electron diffraction [4,5], and ionization-based probes of charge migration [6–10], is expected to benefit from an efficient and accurate theoretical method of calculating SFI in a variety of molecules. In light of this overarching influence of tunnel ionization, it is therefore of paramount importance to have theoretical models that can reliably treat this ionization mechanism.

Highly accurate SFI yields can be obtained by propagating time-dependent wave functions or densities, e.g., using time-dependent *ab initio* methods [11–15], and then recording the amount of density that reaches a predetermined distance far enough from the nuclei to be safely counted as ionized. However, the necessity to employ a basis set that spans distances far from the nuclei means that simulation times for such calculations may be prohibitively long. There have been a number of works focusing on obtaining the ionization probability analytically, i.e., without involving wave-function evolution, such as the Ammosov-Delone-Krainov formulation [16], its molecular version [17], the Keldysh-Faisal-Reiss model [18,19], and the weak-field asymptotic theory (WFAT) [20–22], which may be considered as one of the most successful of this kind of approach (see Refs. [23–25] for comparison with experiments).

Among a number of different types of WFAT developed over the last decade [20–22,26], many-electron WFAT (ME-WFAT) [26] presents several attractive features including that it properly treats the dipole moment during tunneling ionization, uses the actual ionization potential (IP, the difference between neutral and cation eigenvalues) instead of an orbital energy, and is capable of simulating multielectron effects. So far, the ME-WFAT method has been developed in the so-called tail representation (TR) [26], where the wave functions need to have accurate asymptotic behavior. This requirement limits the applicability of ME-WFAT to atoms and diatomic molecules because accurate methods of obtaining orbitals having the correct asymptotic are only available for the above types of molecule [27]. An equivalent formulation in the so-called integral representation (IR) [28] removes the above requirement on having the accurate asymptotic, which has also been developed using the general Hartree-Fock (HF) framework [29]. The reformulation of ME-WFAT within the integral representation makes it capable of further treating tunneling ionization in any molecular geometry. This is presented in Ref. [30] within the HF framework, which can be useful for extending IR ME-WFAT to multiconfiguration

---

[*] These authors contributed equally to this work.
[†] wahyutama1@lsu.edu
[‡] djayas1@lsu.edu

wave functions. However, given that multielectron effects are in general treated very efficiently for a wider class of molecules using density-functional theory (DFT) than multiconfiguration methods, it would be highly desirable to also be able to use DFT wave functions in ME-WFAT calculations.

In this paper, we extend IR ME-WFAT to the framework of DFT wave functions and demonstrate its ability to reproduce angle-dependent ionization yields obtained by real-time time-dependent density-functional theory (RT-TDDFT). The ME-WFAT integral formulas derived using HF orbitals in Ref. [30] are, however, not directly applicable in conjunction with DFT Kohn-Sham orbitals. This is because the functional parametrization in DFT cannot be obtained by starting the analysis from the exact all-electron Hamiltonian without some manual intervention during the derivation. Therefore, in this paper, we will modify the ME-WFAT integral formulas to accommodate the DFT functionals. We will present the ionization yield calculated using the resulting integral formulas for NO, OCS, CH_3Br, and CH_3Cl interacting with two-color and one-color lasers with a fundamental wavelength of 800 nm, and compare them with RT-TDDFT. Here, the time dependence in our WFAT calculations is emulated by adiabatically solving the exponential rate equation for the yield.

We also compare our ME-WFAT results to the one-electron WFAT (OE-WFAT) [20–22,28,31,32]. ME-WFAT differs from OE-WFAT in three main ways: (i) the dipole moment, (ii) the ionization potential, and (iii) the ionizing orbital. While in ME-WFAT one uses the Dyson orbital, in OE-WFAT, the ionizing orbital must be chosen manually from among the occupied molecular orbitals. The ionization potential and dipole moment in OE-WFAT are then taken as orbital energy and dipole moment of the chosen ionizing orbital. The ME-WFAT counterparts of these quantities are taken as the difference between the corresponding neutral and cation values (see Sec. II B). This shows that in OE-WFAT, any information about the cation is absent. Not surprisingly, we will show that ME-WFAT is more accurate than OE-WFAT in many cases presented here. We note that the three methods compared in this paper (ME-WFAT, OE-WFAT, and RT-TDDFT) are only valid for calculations of up to single electron ionization.

We have implemented IR OE-WFAT and ME-WFAT in a development version of the NWCHEM quantum chemistry package [33], which allows for the use of a wide range of basis sets and DFT exchange-correlation (XC) functions. The code is parallelized to handle the computation of some three-dimensional integrals via numerical quadrature, making the simulations scalable to large molecules. Our WFAT implementation requires few additional specifications beyond a standard DFT input, namely, the orbitals of the neutral and cation (for ME-WFAT), the field parameters, and the range of orientation angles. We plan to make our WFAT code publicly accessible by checking into the main branch of the NWCHEM online repository.

The organization of this paper is the following. In Sec. II A, we will provide a brief overview of the ionization calculation using RT-TDDFT. In Sec. II B, the formulation of ME-WFAT using HF orbitals described in Ref. [30] is summarized. The method proposed here, namely, the ME-WFAT using Kohn-Sham orbitals, is outlined in Sec. II C, where the modifications needed to make the HF integral formula in Sec. II B applicable to Kohn-Sham orbitals are presented. Section II D briefly summarizes OE-WFAT by contrasting it with ME-WFAT in several important aspects. The results are presented in Sec. III where we compare the angle-dependent yields obtained by OE-WFAT, ME-WFAT, and full RT-TDDFT simulations. Finally, future potential improvements of the present method are suggested in Sec. IV.

II. OVERVIEW OF THE METHODS

A. RT-TDDFT with CAP

Computationally, SFI is a challenging task because one needs to accurately describe many-electron correlation effects while providing a sufficient representation of the continuum electrons [34]. In this regard, RT-TDDFT provides a balance between the accuracy and speed of the simulation when the system size increases. In a time-dependent Kohn-Sham (TDKS) framework, RT-TDDFT describes electron dynamics in molecular systems by integrating the TDKS equations:

$$i\frac{\partial\psi(\boldsymbol{r},t)}{\partial t} = \left(-\frac{1}{2}\nabla^2 + V_0(\boldsymbol{r},t) + V_H(\rho(\boldsymbol{r},t)) + V_{\mathrm{XC}}(\rho(\boldsymbol{r},t)) - \boldsymbol{D}\cdot\boldsymbol{E}(t)\right)\psi(\boldsymbol{r},t) \tag{1}$$

where $-\frac{1}{2}\nabla^2$ is the kinetic-energy operator for the electrons, V_0 contains the nuclear-electron attraction and the internuclear repulsion, and $\boldsymbol{D}\cdot\boldsymbol{E}(t)$ is the interaction of the transition dipole matrix with the applied external field. Unless otherwise mentioned, we use atomic units throughout this paper. In the adiabatic approximation, the exchange-correlation potential V_{XC} and the electron mean-field repulsion V_H depend only on the instantaneous density denoted by $\rho(\boldsymbol{r},t)$ [35]. Typically, RT-TDDFT simulations start from a ground-state density matrix converged with DFT, but a superposition of nonstationary density matrices can also be used to emulate a sudden excitation [9,10,36,37].

In this paper, we use range-separated hybrid functionals to reduce the self-interaction (SI) error and to get the correct long-range Coulomb potential, which is crucial for ionization calculations [38,39]. Additionally, these functionals can be tuned by varying both the global HF admixture constant α_{RS} and the range-separation parameter γ_{RS} to fulfill Koopman's theorem, i.e., the energy of the highest occupied molecular orbital (HOMO) is equal to the ionization potential of the molecule [38]. For all calculations presented here, we tuned both LC-PBE* and LC-PBE0* functionals [40], which contain pure PBE or PBE0 in the short range and pure HF in the long range. Such a range-based separation of functionals produces the correct long-range behavior of the effective potential, since the HF potential is asymptotically the correct $-1/r$.

The way ionization is treated in our implementation of RT-TDDFT involves two main components: (i) a complex absorbing potential (CAP) placed at some distance from the molecule and (ii) an auxiliary absorbing basis that augments the standard Gaussian one. The CAP distance from the molecule is system dependent and is chosen such that

TABLE I. A summary of some relevant parameters for the simulations presented in this paper. For the functional, hybrid parameters α_{RS} and β_{RS} ($\beta_{\mathrm{RS}} = 1 - \alpha_{\mathrm{RS}}$) are dimensionless whereas γ_{RS}, the range separation parameter, is in units of a.u.$^{-1}$.

Molecule	Functional	$(\alpha_{\mathrm{RS}}, \gamma_{\mathrm{RS}})$	Basis set[a]	CAP (Å)[b]	Simulation time[c]
NO	LC-PBE*	(0.14, 0.55)	N,O : aug-cc-pVTZ + medium	6.5	9.9 h/0.3 m/1.1 m, 192 cores
OCS	LC-PBE0*	(0.0, 0.409)	O,C,S : aug-cc-pVTZ + medium	6.0	28.3 h/3.4 m/4.5 m, 144 cores (N.A./3.4 m/3.1 m, 144 cores)
CH_3Br	LC-PBE0*	(0.7,0.3)	H,Br : aug-cc-pVTZ C : aug-cc-pVTZ + large	7.0	23.0 h/41.7 m/1.4 h, 144 cores (N.A./21.1 m/41.3 m, 288 cores)
CH_3Cl	LC-PBE0*	(0.6, 0.15)	H,Cl : aug-cc-pVTZ C : aug-cc-pVTZ + large	7.0	(N.A./6.5 m/11.5 m, 144 cores)

[a] "Medium" and "large" refer to the medium and large Schlegel absorbing basis, respectively. The corresponding basis set used by WFAT simulations would be the one where the Schlegel absorbing basis is not included.

[b] The distance of the absorbing boundary from the origin.

[c] The times are presented in $t_D/t_O/t_M$ format denoting the simulation times for RT-TDDFT, OE-WFAT, and ME-WFAT, respectively. "The suffixes "h" and "m" mean hours and minutes, respectively." The entries enclosed in parentheses are for simulations with a one-color laser (Sec. III E). The ones not inside parentheses are for two-color laser simulations. All simulation times are for one Euler angle pair.

the ionization rate or yield is insensitive to the CAP position (see Ref. [38] for more details). As for the basis, we use the "medium" and "large" absorbing bases proposed in Ref. [41] augmented to the standard aug-cc-pVTZ basis. This auxiliary basis [41] is what allows the density to reach the CAP as a result of ionization. Although these absorbing bases contain highly diffuse Gaussians, the local nature of Gaussian functions demands the CAP to be placed not too far from the molecule. This causes spurious charge removal even when there is no external field. In all TDDFT simulations performed in this paper, this error has been corrected for following the procedure outlined in Ref. [38]. Unfortunately, these large basis sets have many high angular momentum and diffuse functions. Even for moderately sized molecules, this results in both linear dependencies and significant increases in computational time when evaluating the two-electron integrals. These drawbacks are a strong motivation for finding an efficient alternative approach to TDDFT when possible. The details of tuned functional parameters, CAP positions, and basis sets used in this paper are given in Table I.

B. ME-WFAT using HF orbitals

A full derivation of the angle-dependent ionization yield within the framework of IR ME-WFAT when the wave functions are obtained through the HF method has been given in Ref. [30]. Before presenting the modification required to use these IR ME-WFAT formulas in conjunction with DFT wave functions, we will present a brief overview of WFAT with HF wave functions. Since the HF method has a similar structure to DFT, knowledge of the form of the IR ME-WFAT integral formula for the HF case can help elucidate the reasons why the corresponding formula for DFT requires additional treatment.

The derivation of ME-WFAT in either picture starts from the exact N-electron Schrödinger equation in the presence of a static electric field $\mathbf{F} = F\hat{z}$, that is,

$$H^{(N)}\Psi_n(\mathbf{X}_N) = E_n^{(N)}\Psi_n(\mathbf{X}_N) \tag{2}$$

where

$$H^{(N)} = -\frac{1}{2}\sum_{i=1}^{N}\nabla_i^2 - \sum_{i=1}^{N}\sum_{I=1}^{N_A}\frac{Z_I}{|\mathbf{r}_i - \mathbf{C}_I|} + \sum_{i=1}^{N-1}\sum_{j=i+1}^{N}\frac{1}{|\mathbf{r}_i - \mathbf{r}_j|} + \sum_{i=1}^{N} F z_i,$$

$\mathbf{C}_1, \mathbf{C}_2, \ldots, \mathbf{C}_{N_A}$ are the nuclear coordinates and $Z_1, Z_2, \ldots, Z_{N_A}$ are their charges, and we have used the following notation for the coordinates:

$$\begin{aligned} \mathbf{X}_N &\equiv \{\mathbf{x}_1, \ldots, \mathbf{x}_{N-1}, \mathbf{x}\},\\ \mathbf{R}_N &\equiv \{\mathbf{r}_1, \ldots, \mathbf{r}_{N-1}, \mathbf{r}\},\\ \mathbf{x}_i &\equiv (\mathbf{r}_i, s_i),\\ \mathbf{x} &\equiv \mathbf{x}_N. \end{aligned}$$

Here, $\mathbf{r}_i \equiv (r_i, \theta_i, \varphi_i)$ in spherical coordinates and s_i is the spin coordinate of the ith electron. From this point on, we will assume that the ionized electron has a σ spin projection ($\sigma = a, b$ with $a = 1/2$ and $b = -1/2$), and there are N_σ occupied orbitals (Kohn-Sham orbitals in the case of DFT) in the neutral. We will also denote $\{\psi_1^a, \ldots, \psi_{N_a}^a, \psi_1^b, \ldots, \psi_{N_b}^b\}$ and $\{\upsilon_1^a, \ldots, \upsilon_{N_a'}^a, \upsilon_1^b, \ldots, \upsilon_{N_b'}^b\}$ to be the occupied spin orbitals in the neutral and cation, respectively.

The underlying idea of ME-WFAT is that in the asymptotic region of one of the electrons, the solution of Eq. (2) takes the following ansatz:

$$\Psi_n(\mathbf{X}_N)|_{\eta\to\infty} = \sum_{n'}\Psi_{n'}^{+}(\mathbf{X}_{N-1})\frac{1}{\sqrt{\eta}}\sum_{\nu\sigma} f_{\nu\sigma}^{n'n}\mathcal{L}_{\nu}^{n'n}(\eta, \xi, \varphi)\chi_\sigma(s), \tag{3}$$

where $|\Psi_{n'}^{+}\rangle$ is the solution of the Schrödinger equation analogous to Eq. (2) but defined in the $(N-1)$-electron Hilbert space. $|\chi_\sigma\rangle$ is the spin state having z projection σ, and lastly $\mathcal{L}_{\nu}^{n'n}$ is the one-electron state corresponding to the parabolic channel of $\nu \equiv (n_\xi, m)$ with $n_\xi = 0, 1, \ldots$ and $m = 0, \pm 1, \ldots$. The functional form of $\mathcal{L}_{\nu}^{n'n}[\eta = r + z, \xi = r - z, \varphi = \arctan(y/x)]$ may be deduced from Ref. [30].

The expansion coefficient $f_{\nu\sigma}^{n'n}$ in Eq. (3) describes the amplitude of the channel connecting a neutral eigenstate $|\Psi_n\rangle$

and another state describing the situation where the $N-1$ electrons around the nuclei occupy a cation eigenstate $|\Psi_{n'}^{+}\rangle$, whereas the remaining electron is in a spin-parabolic quantum state $|\mathcal{L}_{\nu}^{n'n}\,\chi_\sigma\rangle$, and is given by

$$\begin{aligned} f_{\nu\sigma}^{n'n} &\approx f_{\nu\sigma}^{(0)}(\mathrm{IP}, F, \beta, \gamma) \\ &= \sqrt{\frac{\varkappa}{2}}\left(\frac{4\varkappa^2}{F}\right)^{\beta_\nu^{(0)}/\varkappa} g_{\nu\sigma}(\beta,\gamma) \\ &\quad\times \exp\left(i\frac{\pi}{4} + i\frac{\pi\beta_\nu^{(0)}}{\varkappa} - \mu_z\varkappa - \frac{\varkappa^3}{3F}\right), \end{aligned} \tag{4}$$

where (β, γ) are the two Euler angles characterizing the orientation of the molecule relative to the field (a more detailed definition of the orientation angles will be given later in Sec. III). Here, the angle β is not to be confused with the spin-down projection defined earlier. Throughout this paper, we will make the distinction explicit when the context is ambiguous. Also, in Eq. (4), $\mathrm{IP} = E^{(N)} - E^{(N-1)}$ is the ionization potential, $\varkappa = \sqrt{2|\mathrm{IP}|}$, μ_z is the z component in the laboratory frame of the vector $\boldsymbol{\mu}^{(N)} - \boldsymbol{\mu}^{(N-1)}$, $\boldsymbol{\mu}^{(N)} = -\langle\Psi|\sum_{i=1}^{N}\hat{\mathbf{r}}_i|\Psi\rangle$ is the electronic dipole moments of the neutral, $\boldsymbol{\mu}^{(N-1)} = -\langle\Psi^+|\sum_{i=1}^{N-1}\hat{\mathbf{r}}_i|\Psi^+\rangle$ is the electronic dipole moment of the cation, $\beta_\nu^{(0)} = Z_c - \varkappa(n_\xi + \frac{|m|+1}{2})$ is the adiabatic eigenvalue [20], and $Z_c = \sum_{I=1}^{N_A} Z_I - N + 1$ is the cation total charge [30]. The approximation in the first line of Eq. (4) corresponds to using the leading-order approximation (LOA) of WFAT. Because of this approximation, all ground-state properties such as wave functions, energies, and dipole moments in the following are associated to the unperturbed systems ($F = 0$).

From this point on, we will omit the eigenstate indices n and n' since HF and DFT produce just one wave function. Here, we follow the authors of Ref. [29] who formulate the *asymptotic coefficient*, $g_{\nu\sigma}$, as

$$g_{\nu\sigma}(\beta,\gamma) = \sum_{l=|m|}^{\infty}\sum_{m'=-l}^{l} I_{\nu l m'\sigma}\, d_{mm'}^{l}(\beta)\, e^{-im'\gamma}, \tag{5}$$

where $d_{mm'}^{l}(\beta)$ is the Wigner function and

$$I_{\nu l m'\sigma} = \left\langle \Psi^+; \Omega_{lm'}^{\nu}\chi_\sigma \middle| \hat{V}_{1e} + \hat{V}_{2e} \middle| \Psi \right\rangle, \tag{6}$$

$$V_{2e}(\mathbf{R}_N) = -\sum_{i=1}^{N-1}\frac{1}{|\mathbf{r}-\mathbf{r}_i|}, \tag{7}$$

$$V_{1e}(\mathbf{r}) = \sum_{I=1}^{N_A}\frac{Z_I}{|\mathbf{r}-\mathbf{C}_I|} - \frac{Z_c}{r}. \tag{8}$$

$I_{\nu l m'\sigma}$ is what we will refer to as the *ME-WFAT integral*. The function $\Omega_{lm'}^{\nu}(\mathbf{r})$ is the solution of the hydrogenlike Schrödinger equation when the energy is not any of the hydrogenlike eigenvalues [29], and is explicitly given by

$$\begin{aligned} \Omega_{lm'}^{\nu}(\mathbf{r}) = {}& \omega_{\nu l}(\varkappa r)^l e^{-\varkappa r} M(l+1-Z/\varkappa, 2l+2, 2\varkappa r) \\ & \times Y_{lm'}(\theta,\varphi), \end{aligned}$$

where $Y_{lm}(\theta,\varphi)$ is the spherical harmonics, $M(a,b,x)$ is the confluent hypergeometric function [42], and $\omega_{\nu l}$ is a normalization factor which may be found in Ref. [29].

The one- and two-electron parts of the ME-WFAT integral of Eq. (6) have been derived in Ref. [30] and are given by

$$\left\langle \Psi^+; \Omega_{lm'}^{\nu}\chi_\sigma \middle| \hat{V}_{1e} \middle| \Psi \right\rangle = \delta_{M_s'+m_\sigma, M_s}\left\langle \Omega_{lm'}^{\nu} \middle| \hat{V}_{1e} \middle| \psi_D^\sigma \right\rangle, \tag{9a}$$

$$\begin{aligned} \left\langle \Psi^+; \Omega_{lm'}^{\nu}\chi_\sigma \middle| \hat{V}_{2e} \middle| \Psi \right\rangle = {}& \frac{\delta_{M_s'+m_\sigma, M_s}}{\sqrt{N}}(-1)^{N+\delta_{\sigma b}N_a} \\ & \times \Bigg\{ \sum_{k'=1}^{N_\sigma-1}\sum_{j=2}^{N_\sigma}\sum_{k=1}^{j-1}\Big(\left\langle \Omega_{lm'}^{\nu} \middle| \hat{J}_{k'k}^{\sigma} \middle| \psi_j^\sigma \right\rangle \\ & -\left\langle \Omega_{lm'}^{\nu} \middle| \hat{K}_{k'k}^{\sigma} \middle| \psi_j^\sigma \right\rangle\Big) + \left\langle \Omega_{lm'}^{\nu} \middle| \hat{\mathcal{V}}^{\sigma} \middle| \tilde{\psi}^\sigma \right\rangle \Bigg\} \end{aligned} \tag{9b}$$

where

$$J_{k'k}^{\sigma}(\mathbf{r}) = (-1)^{j+k+k'}\mathcal{R}\mathcal{Q}(k,j,k')V_{k'k}^{\sigma}(\mathbf{r}), \tag{10}$$

$$\left\langle \mathbf{r} \middle| \hat{K}_{k'k}^{\sigma} \middle| \psi_j^\sigma \right\rangle = (-1)^{j+k+k'}\mathcal{R}\mathcal{Q}(k,j,k')V_{k'j}^{\sigma}(\mathbf{r})\psi_k^\sigma(\mathbf{r}), \tag{11}$$

$$\mathcal{V}^\sigma(\mathbf{r}) = \sum_{k'=1}^{N_{p(\sigma)}}\sum_{k=1}^{N_{p(\sigma)}}(-1)^{k'+k}\mathcal{S}(k',k)V_{k'k}^{p(\sigma)}(\mathbf{r}), \tag{12}$$

$$V_{k'i}^{\sigma}(\mathbf{r}) = \int d^3\mathbf{r}'\left(\upsilon_{k'}^{\sigma}(\mathbf{r}')\right)^*\frac{1}{|\mathbf{r}-\mathbf{r}'|}\psi_i^\sigma(\mathbf{r}'), \tag{13}$$

$$p(\sigma) = \begin{cases} a & ,\sigma = b \\ b & ,\sigma = a \end{cases}. \tag{14}$$

$|\psi_D^\sigma\rangle$ is the Dyson orbital corresponding to the removal of an electron from the spin-σ channel of the neutral, $|\tilde{\psi}^\sigma\rangle$ is a vector related to $|\psi_D^\sigma\rangle$, $\mathcal{Q}(k,j,k')$ is the determinant of the overlap matrix in the *ionized spin channel* between the neutral after removing $\{\psi_k^\sigma, \psi_j^\sigma\}$ and the cation after removing $\{\upsilon_{k'}^\sigma\}$, and $\mathcal{R}$ is the determinant of the overlap matrix in the *unionized spin channel* between the neutral and cation. For more details, we refer the readers to Appendix B. Note that, with Eq. (14), one has $N_\sigma + N_{p(\sigma)} = N$.

As has been shown in Ref. [30], Eq. (9) will reduce to the corresponding equations for OE-WFAT when the cation wave function is formed out of $N-1$ orbitals occupied in the neutral, which is a required property for the formulation so obtained to be mathematically correct. The total angle-dependent ionization rate connecting single-determinantal neutral and cation wave functions is then given by

$$\Gamma(F,\beta,\gamma) \approx \sum_{\sigma\nu} N\left|f_{\nu\sigma}^{(0)}(\mathrm{IP},F,\beta,\gamma)\right|^2 \tag{15}$$

accounting for all probabilities for the ionized electron to reside in all possible parabolic states [26].

C. ME-WFAT using Kohn-Sham orbitals

The reason we need a separate formulation of IR ME-WFAT when the orbitals are of the Kohn-Sham DFT type lies in Eq. (6), which only applies to ME-WFAT used in conjunction with Hartree-Fock wave functions. In what follows, we will outline the reason for this and propose some choices that address the freedom that necessarily occurs when using a parametrized method such as DFT.

First, note that the operator part of the bracket in Eq. (6) lacks the local XC potential term. Second, upon inspection of the two-electron term in Eq. (9b), it can be seen that it also does not have the SI term that makes it possible for the exact exchange in ground-state hybrid DFT calculations to depend on the electronic density. Lastly, in hybrid DFT, one needs to multiply the exact exchange with a positive scalar less than unity. This necessitates a suitable identification of the exact exchange part in the right-hand side of Eq. (9b). With these three observations in mind, one may see that a brute force application of Eq. (6) with DFT orbitals will result in a scheme that has little correspondence with TDDFT. Along with the fact that Koopman's theorem for the ionization potential is not satisfied by approximate DFT functionals (except for tuned range-separated functionals), the resulting scheme also does not reproduce OE-WFAT under the unrelaxed cation orbital situation mentioned shortly after Eq. (9b).

We would like to note that none of the above modifications are needed in OE-WFAT because the derivation of this method can be initiated from the one-electron Kohn-Sham mean-field equation; hence, any DFT-native terms such as the XC potential and the SI term, which are by definition one-particle functions, will automatically be carried over to the OE-WFAT integral formula. This does not apply to ME-WFAT since this method strictly starts off from the exact N-electron Hamiltonian.

To begin the analysis, we impose that the ME-WFAT integral formula for use with DFT orbitals should read

$$I_{\nu l m' \sigma}^{\text{M-DFT}} = \left\langle \Psi^+; \Omega_{lm'}^{\nu} \chi_\sigma \middle| \hat{V}_{1e} + \hat{V}_{2e}^{\text{M-DFT}} + \hat{V}_{\text{SI}} + \hat{V}_{\text{XC}} \middle| \Psi \right\rangle, \quad (16)$$

where Ψ and Ψ^+ are the ground-state DFT wave functions of the neutral and cation, respectively. Given the freedom related to the explicit expressions of these missing parts, we choose to use the unrelaxed cation situation mentioned above as a guide for the construction of the following formulas related to the $\hat{V}_{2e}^{\text{M-DFT}}$, $\hat{V}_{\text{SI}}$, and $\hat{V}_{\text{XC}}$ contributions.

1. *Local exchange-correlation term*

The local exchange-correlation potential lies at the heart of practically every DFT calculation, and is a function of electronic density. Here, within the framework of IR ME-WFAT, we treat this potential as a one-electron potential like the nuclear attraction potential and choose the neutral density (over, for instance, the equally plausible cation density) as the argument of the potential, thus

$$\left\langle \Psi^+; \Omega_{lm'}^{\nu} \chi_\sigma \middle| \hat{V}_{\text{XC}} \middle| \Psi \right\rangle = \delta_{M_s'+m_\sigma, M_s} \left\langle \Omega_{lm'}^{\nu} \middle| \hat{V}_{\text{XC}}(\rho^N) \middle| \psi_D^\sigma \right\rangle. \quad (17)$$

This ensures that this term reduces to the corresponding term in OE-WFAT.

2. *Self-interaction term*

SI is a feature of approximate DFT functionals and describes a situation where the electrons are repelling themselves. The inclusion of SI, which is largely an unphysical mathematical byproduct of the DFT formalism, in our DFT-based ME-WFAT integral is just to facilitate a comparison with TDDFT in which the SI from the exact exchange term is present. In our implementation of the method in the NWCHEM package, the inclusion of the SI term is optional, and may be omitted if desired. To see why SI is missing from Eq. (6), we need to look at Eq. (9b). Inside the triple sum, had the SI terms existed, we should have terms with $k = j$. Introducing such terms into this sum is, however, not straightforward because $\hat{J}_{k'k}^{\sigma}$ and $\hat{K}_{k'k}^{\sigma}$ depend on $\mathcal{Q}(k, j, k')$ [see Eq. (10) and (11)], whereas $\mathcal{Q}(k, j, k')$ is undefined when $j = k$ because in this case, the modified overlap matrix [see Eq. (B1c)] is not square. We therefore propose to use the following expression for the SI term:

$$\left\langle \Psi^+; \Omega_{lm'}^{\nu} \chi_\sigma \middle| \hat{V}_{\text{SI}}^{\text{type I}} \middle| \Psi \right\rangle = \delta_{M_s'+m_\sigma, M_s} \int d^3\mathbf{r}' \left[\Omega_{lm'}^{\nu}(\mathbf{r}')\right]^* \psi_D^\sigma(\mathbf{r}') \times \int d^3\mathbf{r}\, |\tilde{\psi}^\sigma(\mathbf{r})|^2 \frac{1 - w(|\mathbf{r}-\mathbf{r}'|)}{|\mathbf{r}-\mathbf{r}'|} \quad (18)$$

where a general weight function

$$w(y) = \begin{cases} C_X & \text{global exchange} \\ \alpha_{\text{RS}} + \beta_{\text{RS}}\,\text{erf}(\gamma_{\text{RS}}\, y) & \text{RS exchange} \end{cases} \quad (19)$$

has also been inserted to provide applicability of the resulting method to both global and range-separated exchange potentials. The physical motivation behind Eq. (18) is that an electron occupying the Dyson orbital representing the ionization channel of interest feels a repulsion field caused by an electron density due to $\tilde{\psi}^\sigma$, which is proportional to the Dyson orbital [see Eqs. (A3) and (A2)].

We note that there is not a single way to artificially incorporate SI; for instance, the following expression,

$$\begin{aligned} &\left\langle \Psi^+; \Omega_{lm'}^{\nu} \chi_\sigma \middle| \hat{V}_{\text{SI}}^{\text{type II}} \middle| \Psi \right\rangle \\ &\quad = \delta_{M_s'+m_\sigma, M_s} \frac{(-1)^{N+\delta_{\sigma b} N_a}}{\sqrt{N}} \mathcal{R} \\ &\quad\quad \times \int d^3\mathbf{r}' \left\langle \Omega_{lm'}^{\nu}(\mathbf{r}') \right\rangle^* \sum_{i=1}^{N_\sigma} (-1)^i\, \mathcal{P}(i)\, \psi_i^\sigma(\mathbf{r}') \\ &\quad\quad \times \int d^3\mathbf{r}\, \left|\psi_i^\sigma(\mathbf{r})\right|^2 \frac{1 - w(|\mathbf{r}-\mathbf{r}'|)}{|\mathbf{r}-\mathbf{r}'|}, \end{aligned} \quad (20)$$

is equally plausible since, like Eq. (18), Eq. (20) also reduces to the corresponding SI term in OE-WFAT under the unrelaxed cation wave-function condition. In all simulations presented in this paper, we use the first type of SI term, i.e., Eq. (18).

3. *Exact exchange term*

Next, we examine the exact exchange term. To do this requires an inspection of the algebraic structure of Eq. (9b), thus we move the analysis to Appendix C and will simply quote the result here. We require that, first, the occupied molecular orbital in the ionized channel corresponding to the largest absolute value of the coefficient $\mathcal{P}$ is moved to the last index, so that after this reordering one has

$$N_\sigma = \text{argmax}_{i \in [1, N_\sigma]} |\mathcal{P}(i)|. \quad (21)$$

Then, the sought expression for the exact exchange is given by

$$\left\langle \Psi^+; \Omega_{lm'}^{\nu} \chi_\sigma \middle| \hat{V}_{2e}^{\text{M-DFT}} \middle| \Psi \right\rangle$$

$$= \frac{\delta_{M_s'+m_\sigma,M_s}}{\sqrt{N}}(-1)^{N+\delta_{\sigma b}N_a}\Bigg\{\sum_{k'=1}^{N_\sigma-1}\sum_{j=2}^{N_\sigma}\sum_{k=1}^{j-1}\Big(\big\langle\Omega_{lm'}^{\nu}\big|\hat{\mathcal{J}}_{k'k}^{\sigma}\big|\psi_j^{\sigma}\big\rangle - \big\langle\Omega_{lm'}^{\nu}\big|\hat{\mathcal{K}}_{k'k}^{\sigma}\big|\psi_j^{\sigma}\big\rangle\Big) + \big\langle\Omega_{lm'}^{\nu}\big|\hat{\mathcal{V}}^{\sigma}\big|\tilde{\psi}^{\sigma}\big\rangle\Bigg\} \tag{22}$$

with

$$\big\langle\mathbf{r}\big|\hat{\mathcal{K}}_{k'k}^{\sigma}\big|\psi_j^{\sigma}\big\rangle = (-1)^{j+k+k'}\mathcal{R}\mathcal{Q}(k,j,k') \times\left(\int d^3\mathbf{r}'\big[\upsilon_{k'}^{\sigma}(\mathbf{r}')\big]^*\frac{w(|\mathbf{r}-\mathbf{r}'|)}{|\mathbf{r}-\mathbf{r}'|}\psi_j^{\sigma}(\mathbf{r}')\right)\times\psi_k^{\sigma}(\mathbf{r}). \tag{23}$$

In addition to the attainment of the OE-WFAT formula in the case of the unrelaxed cation, the aforementioned reordering that leads to Eq. (21) also ensures that the total angle-dependent yield correctly exhibits the symmetry of the molecule when there are multiple channels having the identical ionization potential, i.e., the case of degenerate ionization channels (see Sec. III D).

D. OE-WFAT using Kohn-Sham orbitals

The application of OE-WFAT with DFT Kohn-Sham orbitals is more straightforward than ME-WFAT because the former is constructed starting from a one-electron eigenvalue problem where DFT terms such as the XC functional and the exact exchange are well defined. In this case, assuming that we choose $\psi_{i'}^{\sigma}$ as the ionizing orbital, the OE-WFAT integral formula reads

$$I_{\nu lm'\sigma}^{\text{O-DFT}} = \big\langle\Omega_{lm'}^{\nu}\big|\hat{V}_{1e}+\hat{V}_{2e}^{\text{O-DFT}}+\hat{V}_{\text{XC}}\big|\psi_{i'}^{\sigma}\big\rangle \tag{24}$$

where $V_{\text{XC}}(\mathbf{r}) = V_{\text{XC}}[\rho^N(\mathbf{r})]$ and

$$\hat{V}_{2e}^{\text{O-DFT}}\big|\psi_{i'}^{\sigma}\big\rangle = \sum_{k=1}^{N_\sigma}\Big(\hat{\mathcal{V}}_{kk}^{\sigma}\big|\psi_{i'}^{\sigma}\big\rangle - \hat{\mathcal{K}}_{kk}^{\sigma}\big|\psi_{i'}^{\sigma}\big\rangle\Big). \tag{25}$$

The explicit form of the exchange term (the second term inside the right-hand-side parentheses) in Eq. (25) is obtained from Eq. (23) using $j = i'$, $k' = k$ [hence $\upsilon_{k'}^{\sigma}(\mathbf{r}) = \psi_k^{\sigma}(\mathbf{r})$], and $\mathcal{R} = \mathcal{Q}(k,i',k) = 1$ [see Eqs. (C1)]. In Eq. (24), there is no need to construct a separate SI term because this effect is already contained in $\hat{V}_{2e}^{\text{O-DFT}}$ [the sum over k in Eq. (25) includes $k = i'$, which is the source of the SI]. The other important differences of OE-WFAT from ME-WFAT are the ionization potential and dipole moment, where in the former, the IP is taken as the orbital energy of the $\psi_{i'}^{\sigma}$ orbital and μ_z is the laboratory-frame z component of the dipole moment of this orbital. The formulation of OE-WFAT, including the definitions of the IP and the dipole moment, makes it clear that OE-WFAT, unlike ME-WFAT, is oblivious to the final state after ionization.

As a reminder, in arriving at Eq. (15) used to calculate the total rate, the channel index [the (n', n) pair] has been dropped due to the use of single determinants in the DFT-based ME-WFAT [see the discussion around Eq. (4)]. In OE-WFAT where the ionizing orbital is chosen manually (hence, the coefficient $f_{\nu\sigma}^{i'(0)}$ depends on i'), it is possible to approximate a given ionization channel starting from the neutral ground state with the ionization from a particular occupied orbital. Therefore, the total rate formula for the DFT-based OE-WFAT is slightly different from Eq. (15) only in the presence of an additional sum over i' and in the absence of the prefactor N.

III. RESULTS AND DISCUSSIONS

We pick four molecules, NO, OCS, CH_3Br, and CH_3Cl, as test beds to gauge how well the WFAT angle-dependent yield reproduces its TDDFT counterpart. But before presenting the ionization yield of these molecules, in Sec. III A, we investigate the intensity dependence of the ionization rates of various channels close to the lowest one in energy (which can be approximated as the ionization from HOMO) to gauge our assumption regarding the importance of the channels other than the lowest one.

We use the same laser field for the WFAT and TDDFT simulations for each molecule. In Secs. III B–III D, this laser is a $(\omega, 2\omega)$ two-color pulse with a sine squared envelope, here $\omega = 0.057$ a.u., which corresponds to a wavelength of 800 nm. The applied external electric field is polarized in the z direction and the relative phase is chosen such that its amplitudes are maximized towards the positive z direction. The advantage of using an asymmetric two-color laser is that the directional dependence of the ionization is probed without ambiguity, since the ionization signal for a given orientation is mostly due to the field in one direction. In Sec. III E, we use a ω one-color laser. The maximum field strength for each molecule is adjusted to be close to the saturation intensity, and the WFAT and TDDFT yields for a given molecule are normalized so that they have identical maximum yield. We adjust the laser peak intensity and duration for each molecular system to make the TDDFT computational times tractable and at the same time to have sufficient number of peaks in the field. Figure 1 shows how the two orientation angles $0^\circ \leqslant \beta \leqslant 180^\circ$ and $0^\circ \leqslant \gamma \leqslant 360^\circ$ determine the orientation of the body-fixed axes relative to the laboratory-fixed axes.

WFAT is, by construction, not a time-dependent method. We can, however, include time dependence quasiadiabatically by solving the exponential decay rate equation

$$\frac{\partial}{\partial t}y(\beta,\gamma,t) = \Gamma(\mathcal{F}(t),\beta,\gamma)[1-y(\beta,\gamma,t)]. \tag{26}$$

Here, $\Gamma(\mathcal{F}(t),\beta,\gamma)$ is the instantaneous total WFAT rate due to a time-varying field $\mathcal{F}(t)$ obtained from Eq. (15) by taking $F = \mathcal{F}(t)$ and $y(\beta,\gamma,t)$ is the quasiadiabatic yield we are interested in. The actual ionization yield $y(\beta,\gamma,t')$ is then calculated at a time t' when the laser pulse has subsided. Equation (26) may be expected to be a good approximation to the actual time-dependent propagation because the field strengths (as confirmed by the amount of ionization) and laser photon energy (≈1.5 eV) are insufficient to cause significant photoexcitation of the system, hence the ionization can be assumed to proceed adiabatically from the ground state. All WFAT results use the same functional type and parameters as TDDFT as shown in Table I. The same basis is also used for each molecule except that the Schlegel absorbing basis is removed for WFAT (see Table I). The Schlegel absorbing basis,

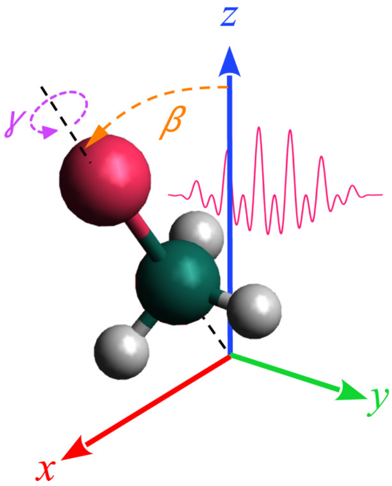

FIG. 1. An illustration of CH_3Br oriented at (β, γ). β and γ are the angles of rotation around the laboratory-fixed y axis and body-fixed z axis, respectively. In this example, the body-fixed z axis (not shown) is along the C–Br bond. The arrows associated with each angle denote the rotation direction corresponding to positive values of the respective angles. The two-color laser pulse is also illustrated where its larger oscillations are always in the positive z direction.

which contains very diffuse functions, is not used for WFAT calculations because we find that the presence of too diffuse functions can make the structure factor incorrectly large. This effect is due to the multiplication of the wave functions with $\Omega^{\nu}_{lm'}$ which increases exponentially with distance [31]. For all simulations here, we use $\nu = \{(0,0), (0,\pm1), (0,\pm2), (1,0)\}$ for the summation in Eq. (15). The angle-dependent yields presented in the following sections were obtained using the OE-WFAT and ME-WFAT modules implemented in the developer version of NWCHEM [33].

A. Field strength dependence of the ionization rates

All of the simulations presented in this paper assume that the dominant ionization corresponds to the ionization channel connecting the ground states of the neutral and of the cation, which is represented by ionization from HOMO in the OE-WFAT framework. It is therefore instructive to ensure that the intensity of the lasers still falls in the region where higher ionization channels (having higher ionization potentials) are still negligible. For this purpose, we run several static field ionization calculations on OCS with varying field strengths using OE-WFAT. The resulting γ-averaged rates are presented in Fig. 2. The range of field strength used in this result covers the peak field value of the laser used in the subsequent sections. As can be seen from Fig. 2, up to $F = 0.05$ a.u., the rate of ionization from HOMO approximately still predominates the higher ionization channels (note that the vertical axis is in logarithmic scale). At $F = 0.02$ a.u., the rate from HOMO is more than four orders of magnitude larger than HOMO-1. The difference between these channels becomes smaller as the field increases, as expected. In particular, the HOMO rate stays separated from the higher channels while they exhibit some crossings at certain angles even when the field is low. This is because HOMO-1, HOMO-2, and HOMO-3 are relatively close in energy (less than ≈1.9 eV apart) while HOMO is 4.9 eV above HOMO-1. This observation serves as the justification of our earlier assumption that for the range of intensity used throughout the subsequent sections, only the lowest (HOMO) ionization channel is important.

B. NO molecule

We start by calculating the angle-dependent ionization yield in the NO molecule. The ionization potential as well as the dipole moment components obtained using the tuned LC-PBE* and aug-cc-pvtz basis are given in Table II, where the internuclear distance is 1.140 Å. Since NO is a radical, an unrestricted Kohn-Sham self-consistent field (SCF) calculation puts the unpaired electron in a particular 2π orbital, which results in an axially asymmetric charge density. This would cause the ionization yield to vary with γ at a given β. A more physical symmetric density may be obtained by smearing the unpaired electron over the two degenerate π orbitals. Instead of doing that, we use the axially asymmetric ground state but average over γ when computing the yield. This averaging of WFAT yields is performed formally, that is,

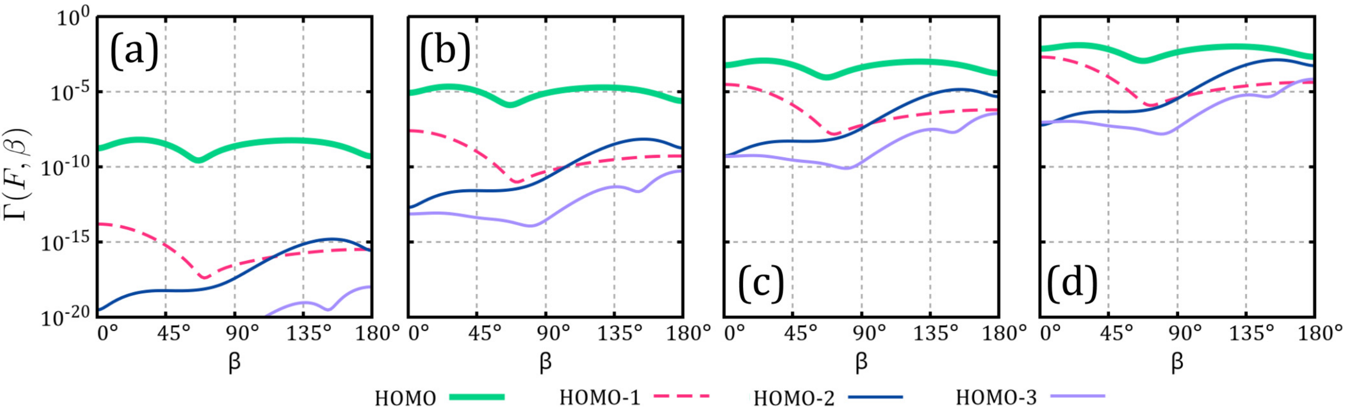

FIG. 2. The average rates, $\bar{\Gamma}_{i'}(F,\beta)$, of some of the high-lying occupied molecular orbitals of OCS as a function of field strength. Here $\bar{\Gamma}_{i'}(F,\beta)$ is calculated as the average of $\sum_{\nu\sigma} |f^{i'(0)}_{\nu\sigma}(\epsilon_{i'}, F, \beta, \gamma)|^2$ over γ, where i' refers to an occupied molecular orbital and $\epsilon_{i'}$ refers to its orbital energy. The field is static and has a magnitude of (a) 0.02 a.u., (b) 0.03 a.u., (c) 0.04 a.u., and (d) 0.05 a.u. calculated using OE-WFAT. The vertical axis is in logarithmic scale.

TABLE II. Ionization potential (in hartree) and the components of $\boldsymbol{\mu}^{(N)} - \boldsymbol{\mu}^{(N-1)}$ (in a.u.) in body-fixed axes, $\tilde{\mu}_x$, $\tilde{\mu}_y$, and $\tilde{\mu}_z$, used in ME-WFAT for NO, OCS, and CH_3Br.

Properties	NO	OCS	CH_3Br
IP	−0.387291	−0.420468	−0.393985
$\tilde{\mu}_x$	0.0	0.0	0.0
$\tilde{\mu}_y$	0.0	0.0	0.0
$\tilde{\mu}_z$	−0.016190	−0.248725	0.811680

for each β we sum the yields over γ and divide the result by 2π. Performing the same averaging for TDDFT yields will, however, be very time consuming due to the large number of (β, γ) pairs. Therefore, for TDDFT yields, the γ averaging is performed in the following manner. We first take an arbitrary fixed β, which is 50° for this simulation, and then average the yields over γ for this β. Having obtained this average value, we look for a γ_{av} still with $\beta = 50^\circ$ that gives the same ionization yield as the average, and we find that $\gamma_{\mathrm{av}} = 324^\circ$. We then fix γ at this value and use it for the scan over β.

The ME-WFAT angle-resolved single ionization yield, averaged over γ, from the NO molecule interacting with a two-color laser having a maximum field of 0.06 a.u. (1.26×10^{14} W/cm^2 in intensity) and a full width at half maximum (FWHM) duration of 22.71 fs is shown in Fig. 3(a). It can be seen to exhibit a butterflylike shape, a characteristic of the dominant orbital contributing to the ionization having π symmetry. In ME-WFAT, the Dyson orbital determines the symmetry of the ionization yield, and indeed, in this calculation it has π symmetry [see inset in Fig. 3(a)]. The relatively low ion yields at $\beta = 0^\circ, 105^\circ, 180^\circ, 255^\circ$ can be explained by the nodes of the Dyson orbital. It has a nodal plane containing the molecular backbone and a nodal cone with an apex located between the nuclei. The yield at these nodal angles is, however, nonzero due to the higher parabolic quantum numbers.

Figure 3(a) also shows the result of TDDFT simulations using identical laser parameters, which are in excellent agreement with the ME-WFAT result. The butterfly-shaped distributions agree with previous experiments [23,43], with the global maxima at $\beta = 50^\circ$ and 310° and secondary maxima at 142° and 218°, measured with respect to the laser polarization direction. Two asymmetric peaks can clearly be distinguished due to the directional asymmetry of the two-color field. It is also worth noting that these angles correspond to the shape of the 2π HOMO as the ionization is preferentially enhanced when the field is directly along a lobe [23].

The angle-dependent yields for ionization from the NO HOMO orbital, computed using OE-WFAT with the same two-color laser, are shown in Fig. 3(b). Here, we see that for NO, ME- and OE-WFAT both yield good agreement with the TDDFT result. In fact, the shape of the HOMO [inset in Fig. 3(b)] is very similar to that of the Dyson orbital in panel (a). The most pronounced disagreement between TDDFT and the two WFAT results is the yield at $\beta = 0^\circ$. As is suggested by our analysis of the HOMO-1 contribution and the effect of the various parabolic channels, we expect that the inclusion of the first-order correction will bring the shape of the yield around $\beta = 0^\circ$ closer to the TDDFT. We note that the WFAT and TDDFT results presented in this section for NO agree with experimental data, also obtained using two-color laser fields [23].

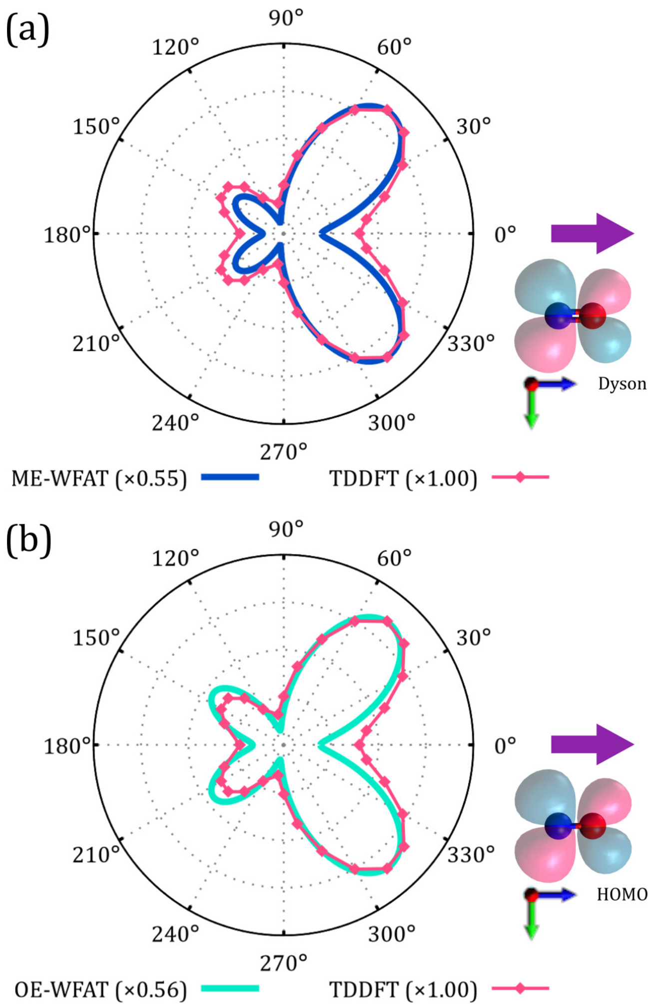

FIG. 3. NO angle-dependent ion yield resulting from an interaction with a laser pulse having 88-TW/cm^2 maximum intensity (0.05-a.u. maximum field) and 22.71-fs FWHM (for this duration, the saturation intensity calculated following Ref. [39] is $I_{\mathrm{sat}} = 220$ TW/cm^2). The ME-WFAT and OE-WFAT results are shown in panel (a) and (b), respectively. The Dyson orbital and HOMO are also shown in panel (a) and (b), respectively. The direction of the largest oscillation of the two-color field is indicated by the purple arrows near the orbitals, which is fixed in the positive z direction as the molecule rotates (the color of the coordinate axes shown below each orbital has the same meaning as that in Fig. 1). The relative orientation between the purple arrow and the orbital indicates its orientation when $\beta = \gamma = 0^\circ$. In this schematic, the left atom is N and the right one is O.

The last column of Table I compares the simulation times for the TDDFT, OE-WFAT, and ME-WFAT calculations for each molecule. We see that for NO, WFAT simulations are more than 100 times faster than TDDFT. We emphasize that the most expensive part of our WFAT algorithm is the calculation of the integrals of Eq. (16), but for a given set of molecule and laser parameters these calculations need be performed only once, while the calculation of ionization rate through the use of Eqs. (4), (5), and (15) for all (β, γ) of interest generally proceeds in just a fraction of the time needed for the preceding integral calculations. So, the times needed to scan all (β, γ) used in the ionization yield plots are just slightly longer than the WFAT times shown in Table I. To perform the same (β, γ) scan in TDDFT would require restarting the TDDFT propagation algorithm for each angle the total cost of which is given by the TDDFT timings shown in Table I times the number of (β, γ) pairs. There are two reasons why WFAT is much faster than TDDFT. First, there is no need to have very diffuse functions in the basis set since the method is not based on propagating the wave function or density to a predetermined, large distance. Second, there is no time evolution algorithm involved. This means that there is no need to repeatedly calculate two-electron integrals needed to construct the Hamiltonian at each time step as in TDDFT.

C. OCS molecule

OCS is a triatomic molecule the equilibrium geometry of which is linear. Like NO, its HOMO, which is doubly degenerate, has π symmetry. There have been some previous attempts at comparing theoretical angle-dependent yields of OCS with experiments with a varying degree of agreement, some of which used single-color linearly polarized laser fields [34,44,45] while another used a circularly polarized laser [46].

The choice of basis and functional mentioned in the beginning of Sec. III produces an ionization potential and dipole moment for OCS given in Table II. The equilibrium geometry for the chosen method and basis occurs at an O-C distance of 1.153 Å and C-S distance of 1.562 Å. For this simulation, a maximum field of 0.045 a.u. (7.1×10^{13} W/cm^2) is used with a FWHM duration of 8.85 fs. The TDDFT yield obtained using these laser parameters is shown with line and markers in Fig. 4, with the maximum found at $\beta = 120^\circ$. At this angle, the laser force component on the electrons along the molecular axis points from O to S. This is consistent with previous experimental and theoretical studies that found a higher ionization rate when the force points from O to S [47], and that the hole ultimately ends up predominantly on the S atom [34].

For the ME-WFAT calculation, it is important to note that the single-determinant ground-state wave functions of OCS$^+$ are doubly degenerate, which can be associated with the π-symmetry HOMO of OCS that is also doubly degenerate. This means one may obtain two different Dyson orbitals (also having π symmetry with lobe directions perpendicular to each other) each corresponding to one of the doubly degenerate cation ground states. By symmetry, the full, unaveraged angle-dependent yields corresponding to these two "degenerate" Dyson orbitals are trivially connected by a 90° shift of γ. Since the ionization potentials for these two degenerate channels are identical, one should sum the ME-WFAT rates of these two channels to obtain the total rate, which results in a corresponding total yield that is independent of γ. Before moving on, we would like to emphasize that the neglect of the reordering procedure described in Sec. II C 3 will result in the absence of this axial symmetry in the full OCS angle-dependent ionization yield.

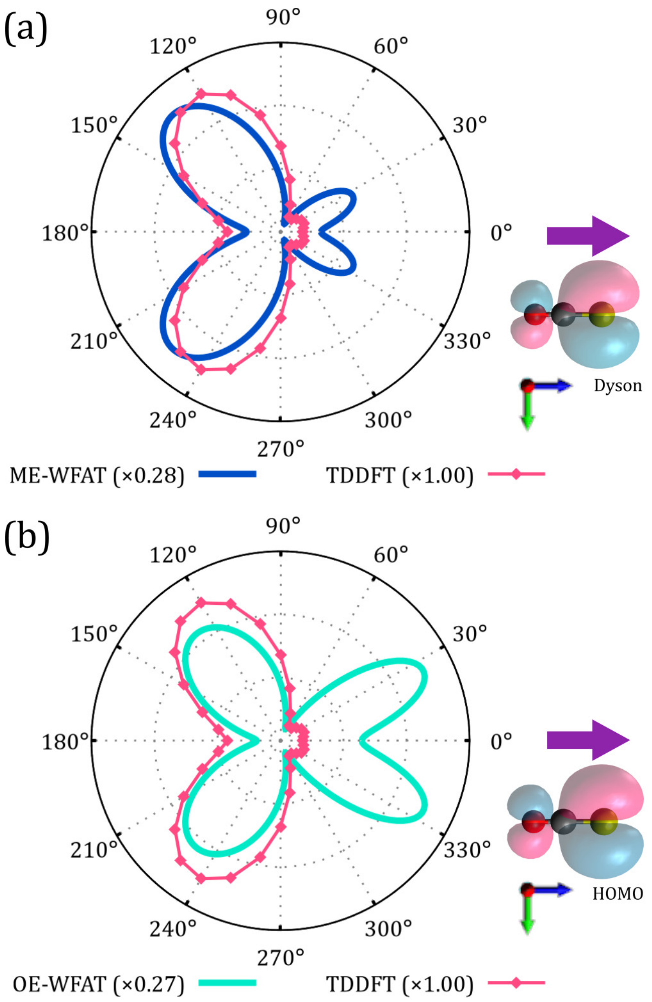

FIG. 4. OCS angle-dependent ion yield comparing (a) ME-WFAT and (b) OE-WFAT with TDDFT results. The laser pulse has 65-TW/cm^2 maximum intensity (0.043-a.u. maximum field) and 8.85-fs FWHM ($I_{\mathrm{sat}} = 176$ TW/cm^2). The meanings of the purple arrow, the orbital image, and the coordinate axes are the same as those in Fig. 3. In the ball-and-stick representation of the molecule, the left atom is O and the right one is S.

The ME-WFAT ionization yield [solid line in Fig. 4(a)] is seen to have a reasonably good agreement with the TDDFT yield (line with marker), with a small difference in the location of the global maxima and in the more pronounced secondary maxima at around $\beta = 30^\circ$ and 330°. A possible reason for the latter is the effect of induced core polarization, which has recently been studied in Refs. [48,49]. In this mechanism, the external field polarizes the core electron density so that the charge imbalance of the latter creates a counteracting internal field that can substantially decrease the net field for a given orientation, leading to a very low yield around that orientation. This dynamical effect is not captured by the LOA employed in our ME-WFAT formulation, but can be treated by including the first-order correction to ME-WFAT [50].

The OE-WFAT ionization yield is shown in Fig. 4(b). In contrast to the NO case, the OE-WFAT ionization yield does not agree qualitatively with the TDDFT result due to the peak at 30° and 330° now becoming the global maximum, although the Dyson orbital and HOMO are still very similar (see the orbital images in Fig. 4). Such a disagreement is caused by the incorrect dipole moment used by the OE-WFAT to describe the ionization probability connecting the initial neutral state to the final cation state. For comparison, the reader is referred to the respective explanations for dipole moment in the paragraphs after Eq. (4) and after Eq. (25). Reference [30] presents some examples where the main factor dictating the difference of the ME-WFAT and OE-WFAT yields also comes from the shape of the ionizing orbital, i.e., where the Dyson orbital is notably different from the HOMO. It is worth mentioning that the solid line in Fig. 4(b) is very similar to the OCS structure factor shown in Fig. 11 of Ref. [31]. Finally, we note that the computational times for OCS in Table I show that WFAT is, as expected, much faster (about 150 times faster) than full TDDFT simulations.

D. CH_3Br molecule

Bromomethane has C_{3v} symmetry and possesses a threefold rotational symmetry around the C–Br bond. The properties of this molecule relevant to ME-WFAT are given in Table II. The atomic coordinates can be deduced from Table IV of Ref. [39] since the same basis and functional are used here.

Similar to the case of OCS above, the single-determinant ground-state wave functions of CH_3Br^+ and the HOMO of CH_3Br are both doubly degenerate (see the two orbital pairs in Fig. 5). This means the Dyson orbital is also doubly degenerate. We obtain the doubly degenerate CH_3Br^+ ground states by using $N-1$ neutral orbitals, removing one of its two degenerate HOMOs as the starting guess for the cation's SCF iteration. We identify the two states in these degenerate manifolds (the HOMO and the Dyson orbital) using their reflection symmetry with respect to any of the Br–C–H planes. The one that is even (odd) under this reflection is denoted with the + (–) sign (see the orbital images in Fig. 5).

The full, unaveraged ME-WFAT ionization yields starting from CH_3Br in the ground state and ending up in the two degenerate ground states of CH_3Br^+ are shown in Figs. 6(a) and 6(b). Here, the ionizing field is a two-color laser with a field maximum of 0.05 a.u. (8.8×10^{13} W/cm^2) and an intensity FWHM of 13.18 fs. The total yield, shown in Fig. 6(c), is the sum of the yields corresponding to the degenerate cation final states in Figs. 6(a) and 6(b). Here, we observe a 120° periodicity along the γ axis of the yield, which is a reflection of the threefold rotational symmetry of CH_3Br around the C-Br bond. Again, the neglect of the reordering procedure described in Sec. II C 3 will result in the absence of the threefold rotational symmetry seen in Fig. 6(c).

The γ average of the yield in Fig. 6(c) is shown in Fig. 5(a) as a solid line. For the TDDFT yield, the same averaging method as in Sec. III B for NO is also employed here, where we set $\beta=120^\circ$, perform an average over γ, and find $\gamma_{\rm av}$ that gives identical ionization yield as this average. This procedure yields $\gamma_{\rm av}=36^\circ$ as the value to be used for the subsequent scan over β. A comparison of ME-WFAT (solid line) and the TDDFT yields (dashed line) in Fig. 5(a) tells us that ME-WFAT is again a reliable alternative to TDDFT for calculating angle-resolved ionization. The ME-WFAT yield in Fig. 5(a) also looks similar to the result of a previous work on CH_3Br interacting with a static field simulated using the time-dependent configuration interaction [51].

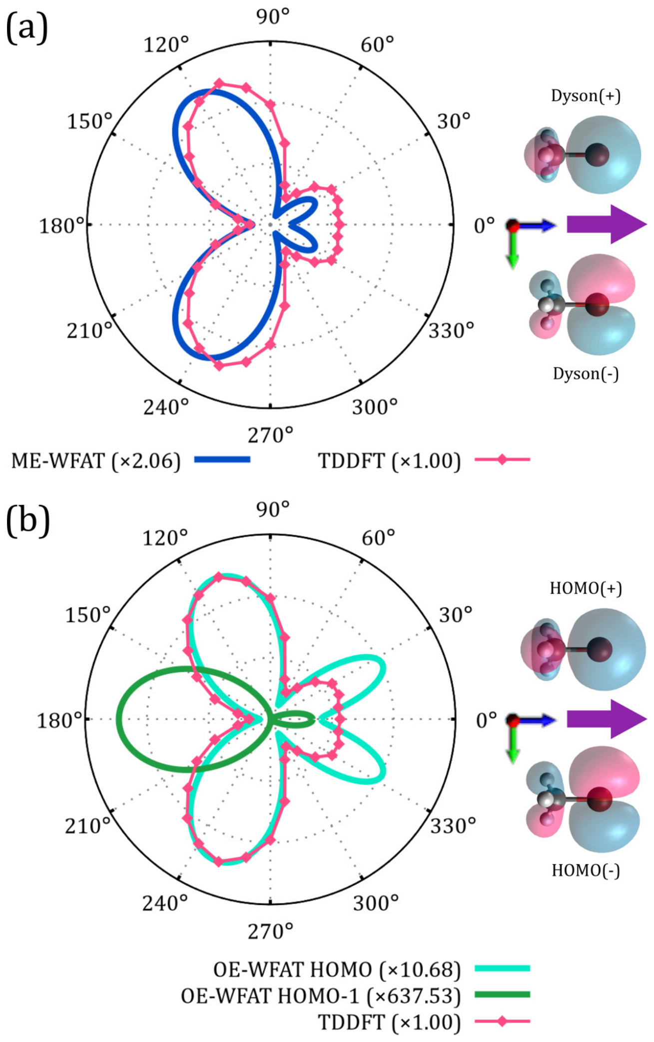

FIG. 5. CH_3Br angle-dependent ion yield comparing (a) ME-WFAT and (b) OE-WFAT with TDDFT results. The laser pulse has 43-TW/cm^2 maximum intensity (0.035-a.u. maximum field) and 13.18-fs FWHM ($I_{\rm sat}=150$ TW/cm^2). The meanings of the purple arrow, the orbital image, and the coordinate axes are the same as those in Fig. 3. In the ball-and-stick representation of the molecule, the right atom is Br and the middle one is C.

The angle-dependent yield obtained using OE-WFAT is shown in Fig. 5(b) as a thick solid line. The shapes of the maxima peaking at 111° and 249° have a better agreement with those of TDDFT, but the strength of the secondary maxima at 26° and 334° is almost twice as large as the corresponding TDDFT values.

Figure 5(a) reveals that the biggest discrepancy between TDDFT and ME-WFAT yields lies around $\beta=0^\circ$. We identify two possible reasons to this: (1) the contribution of the ionization channel connecting the neutral ground state to the cation first excited state (or in the OE-WFAT framework, the contribution of HOMO-1) and (2) the orbital distortion effect. The first possibility, however, cannot be investigated using ME-WFAT with DFT orbitals since the excited-state wave

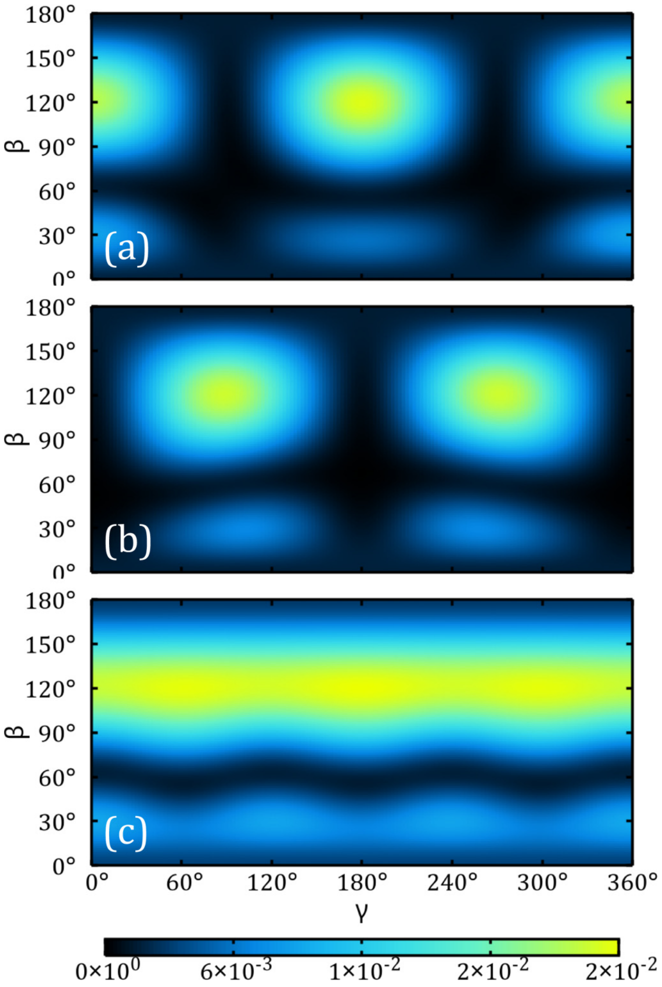

FIG. 6. The full two-dimensional CH_3Br angle-dependent ionization yield. The yields due to each of the doubly degenerate Dyson orbitals are shown in panel (a) and (b). Panel (c) shows the total yield.

function requires a multideterminant description. Instead, we use OE-WFAT using the HOMO-1 orbital as the ionizing orbital to shed some light, albeit less accurately. We identify that HOMO-1 has a σ-like character. The resulting ionization yield is shown in Fig. 5(b) denoted as HOMO-1 in which we see that the yield at $\beta = 0^\circ$ is nonzero for this contribution. Note that the relative magnitude between the yields at $\beta = 0^\circ$ and 180° in the HOMO-1 contribution is the opposite of that in the TDDFT yield which is greater at $\beta = 0^\circ$. Also, the difference in the magnitude between HOMO and HOMO-1 (compare the scaling factors) looks to be too big to warrant noticeable effect of the latter around $\beta = 0^\circ$. We attribute these seemingly contradicting behaviors to the inaccuracy of OE-WFAT.

The second possibility, the orbital distortion due to the laser, is not possible to simulate using the current version of DFT-based ME-WFAT as it requires extending the current formalism to include the first-order correction. Aside from this small difference at $\beta = 0^\circ$, the overall shape of the ME-WFAT angle-dependent yield agrees qualitatively with TDDFT.

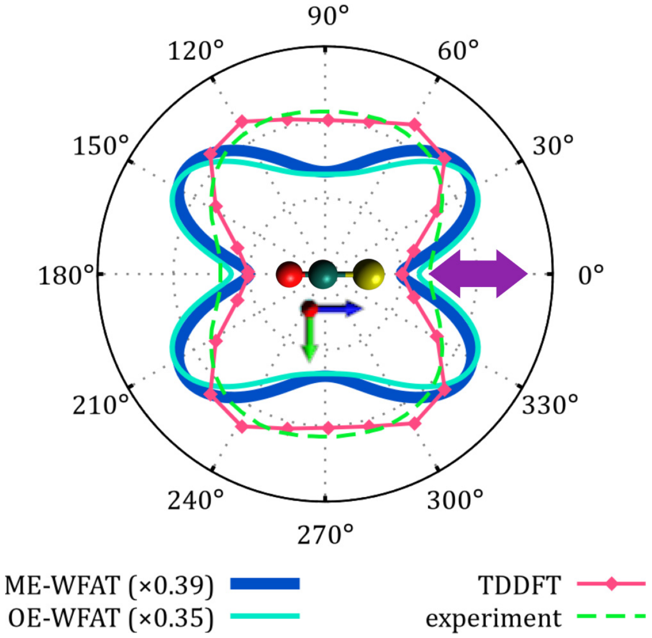

FIG. 7. OCS angle-dependent ionization yields due to a one-color laser. The peak (saturation) intensity is 70 TW/cm^2 (80 TW/cm^2), with a FWHM duration of 37 fs. The relative orientation between the molecule, the laser field polarization (purple arrow), and the coordinate axes as shown indicates the orientation when $\beta = \gamma = 0^\circ$. Additionally, TDDFT calculations and experimental measurement extracted from Ref. [34] are also plotted. The WFAT values are scaled so that their maxima coincide with the maximum of the TDDFT yield.

E. One-color ionization from OCS, CH_3Cl, and CH_3Br

In this section, we provide further results demonstrating the capability of ME-WFAT to efficiently reproduce the more accurate TDDFT calculations and available experimental data. Figure 7 shows the ionization yield for OCS interacting with a one-color sine-squared pulse having a wavelength of 800 nm and an intensity FWHM of 37 fs obtained by ME-WFAT, OE-WFAT, and TDDFT, and from experimental data extracted from Ref. [34]. The peak intensity is 70 TW/cm^2. For this case, we observe a notable discrepancy between WFAT and TDDFT or experiment. We attribute this to the difference in the loci of the global maxima in Fig. 4(a) for ME-WFAT and to the difference of the yield values around $\beta = 30^\circ$ and 330° in Figs. 4(a) and 4(b) for both WFAT results. We expect that this disagreement in the case of OCS will be remedied by the inclusion of the first-order correction to WFAT.

Figure 8 shows the angle-dependent ionization of (a) CH_3Cl and (b) CH_3Br interacting with a one-color laser having the same parameters as those used to obtain Fig. 7 except that the peak intensity for panel (a) is 64 TW/cm^2 and for panel (b) it is 60 TW/cm^2. The experimental data are extracted from Ref. [39]. The range-separated functional parameters and basis used in Fig. 8(a) are given in Table I.

As shown in Fig. 8, ME-WFAT yields produce a much better agreement with TDDFT as well as experiment compared to OE-WFAT results. In particular, for CH_3Cl, the peaks in both TDDFT and ME-WFAT within the range of $0 \leqslant \beta \leqslant 180^\circ$ are located at 45° and 135°, whereas in the same β interval,

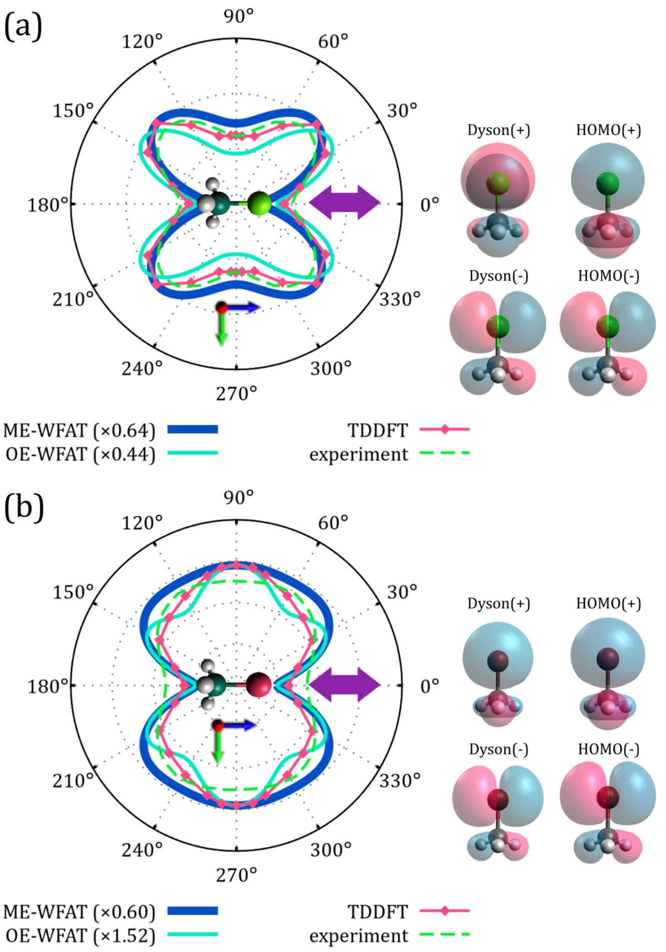

FIG. 8. (a) CH_3Cl and (b) CH_3Br angle-dependent ionization yields due to a one-color laser. The peak (saturation) intensity for panel (a) is 64 TW/cm^2 (80 TW/cm^2), whereas for panel (b) it is 60 TW/cm^2 (50 TW/cm^2), with a FWHM duration of 37 fs for both. In the ball-and-stick representation of the molecule, the right atom is the halogen. The relative orientation between the molecule, the laser field polarization (purple arrow), and the coordinate axes as shown indicates the orientation when $\beta = \gamma = 0^\circ$. Additionally, TDDFT calculations and experimental measurement extracted from Ref. [39] are also plotted. The WFAT values are scaled so that their maxima coincide with the maximum of the TDDFT yield. The Dyson orbitals (used in ME-WFAT) and HOMO (used in OE-WFAT) are also shown.

OE-WFAT produces peaks at 35° and 145°. In the case of CH_3Br, both TDDFT and ME-WFAT yields have a smooth shape in the range of $0 \leqslant \beta \leqslant 180^\circ$ while OE-WFAT features three separated peaks. The peaks at 33° and 147° are mainly contributed by the secondary maxima around the same angle seen in the OE-WFAT(HOMO) yield in Fig. 5(b).

The qualitative difference in the shape of the yields between CH_3Cl and CH_3Br, especially the fact that at 90° and 270° CH_3Br features maxima while CH_3Cl features minima, can be related to the shape of the orbitals. In particular, we see from both the HOMO and Dyson orbitals of the two molecules that the relative electron density in the region around the halogen to that around the hydrogens is higher when the halogen is Br rather than Cl.

IV. CONCLUSION AND OUTLOOK

In this paper, we have demonstrated that ME-WFAT in the LOA is a promising alternative which, when combined with a quasiadiabatic treatment of the electric field using Eq. (26), produces an efficient and accurate method for calculating tunnel ionization in the adiabatic regime. We emphasize that the application of ME-WFAT for the general molecular case as presented here is made possible by reformulating the TR [26] in the IR [30]. In the IR, one can bypass the need for having the accurate exponentially decaying tail of the orbitals, which is only reliably possible for atoms and diatomic molecules [27].

We have applied the LOA of IR ME-WFAT that has been derived in Ref. [30] for Hartree-Fock orbitals to the case of DFT Kohn-Sham orbitals. The use of Kohn-Sham orbitals in ME-WFAT requires modification of the ME-WFAT formula to include missing terms such as the XC potential and the self-interaction terms, as well as identifying a suitable exact exchange term. Several reformulations are possible in the expression of each of the aforementioned terms, which can be attributed to the parametrization of DFT. By comparing the ME-WFAT against TDDFT angle-dependent yields, we showed that the particular choice of these expressions proposed in this paper is indeed suitable.

We have chosen to study the molecules NO, OCS, CH_3Br, and CH_3Cl interacting with either one-color or two-color laser pulses to test the reliability of ME-WFAT as an alternative method for the calculation of tunnel ionization. In all these cases, we showed that ME-WFAT is able to reproduce TDDFT angle-dependent ionization yields, whereas OE-WFAT is only able to do so for NO. While for NO, ME-WFAT and TDDFT are in excellent agreement, the most noticeable difference between ME-WFAT and TDDFT in the case of OCS and CH_3Br lies in the region around $\beta = 0^\circ$. For OCS, the most likely reason is the induced polarization of the core orbitals, which is not captured by ME-WFAT, whereas for CH_3Br, we attribute this difference to the significant contribution of the ionization channel connecting a neutral ground state and a certain cation excited state around $\beta = 0^\circ$. The overall qualitatively good agreement between the quasistatic WFAT and RT-TDDFT simulations indicates that the ionized electron can be treated using an adiabatic description for wavelengths as short as 800 nm. On the other hand, one may expect that WFAT is insufficient to treat nonadiabatic processes, such as interchannel coupling during ionization and carrier-envelope phase effects. The very efficient nature of WFAT simulations (see the timings in Table I) also makes it a fitting candidate as a tool to perform a quick scan of the ionization properties of large molecules before more elaborate calculations or actual experiments are conducted on them.

One direction for improvement of our results would be the inclusion of the first-order correction to ME-WFAT. This correction accounts for the distortion of orbitals due to the field, which may be needed to correct for the OCS disagreement discussed above. Such an effort for ME-WFAT in the tail representation has been outlined in Ref. [50]. An appealing application for ME-WFAT may be to the study of particlelike charge migration [9,10,36] where it is shown that an initial localized hole can sustain its locality throughout the periodic dynamics. Given the coupled time-space sensitivity of such a dynamic, IR ME-WFAT opens up a promising avenue in the modeling of tunnel ionization as a probe of charge migration.

ACKNOWLEDGMENTS

We thank Oleg Tolstikhin for the enlightening discussion about WFAT. The authors are also grateful to Takeshi Sato for his suggestions regarding the degenerate Hartree-Fock solutions of CH_3Br^+. We also thank Peter Sándor and Robert Jones for their permission to use their data in our paper, and Adonay Sissay for his help with some simulation parameters. This work is supported by the U.S. Department of Energy, Office of Science, Office of Basic Energy Sciences, under Grant No. DE-SC0012462. Portions of this research were conducted with high-performance computational resources provided by Louisiana State University [52] and the Louisiana Optical Network Infrastructure [53].

APPENDIX A: DYSON ORBITAL FOR SINGLE-DETERMINANT WAVE FUNCTIONS

When both of the neutral and cation wave functions are a single determinant, that is,

$$\Psi(\mathbf{X}_N) = \frac{1}{\sqrt{N!}} \det\left(\psi_1^a \cdots \psi_{N_a}^a \, \psi_1^b \cdots \psi_{N_b}^b\right), \tag{A1a}$$

$$\Psi^+(\mathbf{X}_{N-1}) = \frac{1}{\sqrt{(N-1)!}} \det\left(\upsilon_1^a \cdots \upsilon_{N_a'}^a \, \upsilon_1^b \cdots \upsilon_{N_b'}^b\right), \tag{A1b}$$

then the Dyson orbital may be shown to have the form

$$\begin{aligned}\psi_D^\sigma(\mathbf{r}) &= \int d\mathbf{X}_{N-1} d\sigma' \, [\Psi^+(\mathbf{X}_{N-1})]^* \Psi(\mathbf{X}_{N-1}, \mathbf{r}\sigma') \\ &= \frac{(-1)^{N+\delta_{\sigma b} N_a}}{\sqrt{N}} \mathcal{R} \, \tilde{\psi}^\sigma(\mathbf{r}),\end{aligned} \tag{A2}$$

where

$$\tilde{\psi}^\sigma(\mathbf{r}) = \sum_{i=1}^{N_\sigma} (-1)^i \mathcal{P}(i) \psi_i^\sigma(\mathbf{r}). \tag{A3}$$

σ is the ionized spin channel, that is, the spin channel of the neutral from which an electron has been removed, and $\mathcal{P}(i)$ and $\mathcal{R}$ are defined in Appendix B. Equation (A2) assumes that the following conditions constraining the number of electrons in each spin channel of both the neutral and cation,

$$N_\sigma' = N_\sigma - 1,$$
$$N_{p(\sigma)}' = N_{p(\sigma)},$$

are satisfied. These relations are the consequence of single-determinant wave functions being an eigenstate of the z component of spin angular momentum. If not, the Dyson orbital uniformly vanishes.

APPENDIX B: VARIOUS OVERLAP INTEGRALS BETWEEN NEUTRAL AND CATION WAVE FUNCTIONS

Letting $S_\sigma^{\Psi^+\Psi}[a', b', \ldots | a, b, \ldots]$ be the spin-σ block of the overlap matrix formed between the orbitals occupied in $|\Psi^+\rangle$ removing spin orbitals $a', b', \ldots$ and the orbitals occupied in $|\Psi\rangle$ removing spin orbitals $a, b, \ldots$, then

$$\mathcal{P}(i) = \det\left(S_\sigma^{\Psi^+\Psi}\left[\varnothing \middle| \psi_i^\sigma\right]\right), \tag{B1a}$$

$$\mathcal{R} = \det\left(S_{p(\sigma)}^{\Psi^+\Psi}\left[\varnothing \middle| \psi_i^\sigma\right]\right), \tag{B1b}$$

$$\mathcal{Q}(k, i, k') = \det\left(S_\sigma^{\Psi^+\Psi}\left[\upsilon_{k'}^\sigma \middle| \psi_i^\sigma, \psi_k^\sigma\right]\right)(1 - \delta_{ik}), \tag{B1c}$$

$$\mathcal{S}(k, k') = \det\left(S_{p(\sigma)}^{\Psi^+\Psi}\left[\upsilon_{k'}^{p(\sigma)} \middle| \psi_i^\sigma, \psi_k^{p(\sigma)}\right]\right), \tag{B1d}$$

where the notation $\varnothing$ means that no orbitals are removed from the corresponding charge state. A full derivation on how these determinants arise within the formulation of IR ME-WFAT will be presented in Ref. [30].

APPENDIX C: EXCHANGE TERM IN THE ME-WFAT INTEGRAL

At first glance, it might be tempting to identify the $\hat{K}_{k'k}^\sigma$ term in Eq. (9b) as the exchange term. In this section we will first show that this is not the case, and then analyze Eq. (9b) to identify the most suitable term to be regarded as the exchange term in the context of IR ME-WFAT using DFT Kohn Sham orbitals. As a guide, we use ME-WFAT with HF and in the case of unrelaxed cation orbitals, which are just taken from $N-1$ occupied orbitals of the neutral. We also assume the only neutral orbital unoccupied in the cation to be $\psi_{i'}^\sigma$. In this case,

$$\mathcal{P}(i) = \delta_{ii'}, \tag{C1a}$$

$$\mathcal{R} = 1, \tag{C1b}$$

$$\mathcal{Q}(k, i, k') = (1 - \delta_{ik})(\delta_{ii'}\delta_{k'\bar{k}} + \delta_{ki'}\delta_{k'\bar{i}}), \tag{C1c}$$

$$\mathcal{S}(k, k') = \delta_{k'k}. \tag{C1d}$$

Using Eq. (C1) in the triple sum of Eq. (9b), one obtains

$$\begin{aligned}&\sum_{k'=1}^{N_\sigma-1} \sum_{j=2}^{N_\sigma} \sum_{k=1}^{j-1} \left(\hat{J}_{k'k}^\sigma \middle|\psi_j^\sigma\right\rangle - \hat{K}_{k'k}^\sigma \left|\psi_j^\sigma\right\rangle\Big) \\ &= \sum_{k'=1}^{N_\sigma-1} \sum_{k=1}^{i'-1} (-1)^{k+k'} \delta_{k'k} \Big(\hat{V}_{k'k}^\sigma \left|\psi_{i'}^\sigma\right\rangle - \hat{V}_{k'i'}^\sigma \left|\psi_k^\sigma\right\rangle\Big) \\ &\quad + \sum_{k'=1}^{N_\sigma-1} \sum_{k=i'+1}^{N_\sigma} (-1)^{k+k'} \delta_{k',k-1} \Big(\hat{V}_{k'i'}^\sigma \left|\psi_k^\sigma\right\rangle - \hat{V}_{k'k}^\sigma \left|\psi_{i'}^\sigma\right\rangle\Big) \\ &= \sum_{k\neq i'}^{N_\sigma} \Big(\hat{V}_{kk}^\sigma \left|\psi_{i'}^\sigma\right\rangle - \hat{V}_{ki'}^\sigma \left|\psi_k^\sigma\right\rangle\Big),\end{aligned} \tag{C2}$$

where we note that the last expression is just the classical repulsion and exchange terms among electrons with the same spin in the OE-WFAT integral formula.

A closer look at the first and second lines of the right-hand side reveals that there are certain pairs of (j, k) from both the $\hat{J}_{k'k}^\sigma$ and $\hat{K}_{k'k}^\sigma$ terms on the left-hand side that lead to the exchange (second) term in the third line. In particular, on the right-hand side, the second term inside the parentheses of the first line plus the first term inside the parentheses of the second line together constitute the exchange term in the third line. This is why in general one cannot assign $\hat{K}_{k'k}^\sigma$ alone as the exchange in the ME-WFAT integral. We can, however, identify an occupied orbital of the neutral that is "most similar" to the Dyson orbital. The most straightforward method of this identification is by finding the largest absolute value of the elements of $\mathcal{P}(i)$, which, in most cases, corresponds to $\psi^{\sigma}_{i'}$. Then by reordering the neutral orbitals such that this largest element is at N_σ (that is, $i' = N_\sigma$), we can eliminate the second term on the right-hand side of Eq. (C2) (the third line). After this reordering, one can identify the $\hat{K}^{\sigma}_{k'k}$ term in the left-hand side of this equation as the exchange contribution.

[1] A. McPherson, G. Gibson, H. Jara, U. Johann, T. S. Luk, I. A. McIntyre, K. Boyer, and C. K. Rhodes, Studies of multiphoton production of vacuum-ultraviolet radiation in the rare gases, J. Opt. Soc. Am. B **4**, 595 (1987).

[2] J. L. Krause, K. J. Schafer, and K. C. Kulander, Calculation of photoemission from atoms subject to intense laser fields, Phys. Rev. A **45**, 4998 (1992).

[3] P. Eckle, A. N. Pfeiffer, C. Cirelli, A. Staudte, R. Dörner, H. G. Muller, M. Büttiker, and U. Keller, Attosecond ionization and tunneling delay time measurements in helium, Science **322**, 1525 (2008).

[4] C. I. Blaga, J. Xu, A. D. DiChiara, E. Sistrunk, K. Zhang, P. Agostini, T. A. Miller, L. F. DiMauro, and C. D. Lin, Imaging ultrafast molecular dynamics with laser-induced electron diffraction, Nature (London) **483**, 194 (2012).

[5] A. Sánchez, K. Amini, S.-J. Wang, T. Steinle, B. Belsa, J. Danek, A.-T. Le, X. Liu, R. Moshammer, T. Pfeifer, M. Richter, J. Ullrich, S. Gräfe, C. D. Lin, and J. Biegert, Molecular structure retrieval directly from laboratory-frame photoelectron spectra in laser-induced electron diffraction, Nat. Commun. **12**, 1520 (2021).

[6] F. Calegari, D. Ayuso, A. Trabattoni, L. Belshaw, S. D. Camillis, S. Anumula, F. Frassetto, L. Poletto, A. Palacios, P. Decleva, J. B. Greenwood, F. Martín, and M. Nisoli, Ultrafast electron dynamics in phenylalanine initiated by attosecond pulses, Science **346**, 336 (2014).

[7] E. P. Månsson, S. Latini, F. Covito, V. Wanie, M. Galli, E. Perfetto, G. Stefanucci, H. Hübener, U. De Giovannini, M. C. Castrovilli, A. Trabattoni, F. Frasetto, L. Poletto, J. B. Greenwood, F. Légaré, M. Nisoli, A. Rubio, and F. Calegari, Real-time observation of a correlation-driven sub 3 fs charge migration in ionised adenine, Commun. Chem. **4**, 73 (2021).

[8] A. Bruner, S. Hernandez, F. Mauger, P. M. Abanador, D. J. LaMaster, M. B. Gaarde, K. J. Schafer, and K. Lopata, Attosecond charge migration with TDDFT: Accurate dynamics from a well-defined initial state, J. Phys. Chem. Lett. **8**, 3991 (2017).

[9] A. S. Folorunso, A. Bruner, F. Mauger, K. A. Hamer, S. Hernandez, R. R. Jones, L. F. DiMauro, M. B. Gaarde, K. J. Schafer, and K. Lopata, Molecular Modes of Attosecond Charge Migration, Phys. Rev. Lett. **126**, 133002 (2021).

[10] F. Mauger, A. S. Folorunso, K. A. Hamer, C. Chandre, M. B. Gaarde, K. Lopata, and K. J. Schafer, Charge migration and attosecond solitons in conjugated organic molecules, Phys. Rev. Res. **4**, 013073 (2022).

[11] J. Zanghellini, M. Kitzler, C. Fabian, T. Brabec, and A. Scrinzi, An MCTDHF approach to multielectron dynamics in laser fields, Laser Phys. **13**, 1064 (2003).

[12] T. Kato and H. Kono, Time-dependent multiconfiguration theory for electronic dynamics of molecules in an intense laser field, Chem. Phys. Lett. **392**, 533 (2004).

[13] L. Greenman, P. J. Ho, S. Pabst, E. Kamarchik, D. A. Mazziotti, and R. Santra, Implementation of the time-dependent configuration-interaction singles method for atomic strong-field processes, Phys. Rev. A **82**, 023406 (2010).

[14] T. Sato and K. L. Ishikawa, Time-dependent complete-active-space self-consistent-field method for multielectron dynamics in intense laser fields, Phys. Rev. A **88**, 023402 (2013).

[15] H. Miyagi and L. B. Madsen, Time-dependent restricted-active-space self-consistent-field theory for laser-driven many-electron dynamics, Phys. Rev. A **87**, 062511 (2013).

[16] M. V. Ammosov, N. B. Delone, and V. P. Krainov, Tunnel ionization of complex atoms and atomic ions in electromagnetic field, in *High Intensity Laser Processes*, SPIE Proceedings Vol. 0664, edited by J. A. Alcock (SPIE, Bellingham, WA, 1986), pp. 138–141.

[17] X. M. Tong, Z. X. Zhao, and C. D. Lin, Theory of molecular tunneling ionization, Phys. Rev. A **66**, 033402 (2002).

[18] H. R. Reiss, Effect of an intense electromagnetic field on a weakly bound system, Phys. Rev. A **22**, 1786 (1980).

[19] J. Muth-Böhm, A. Becker, and F. H. M. Faisal, Suppressed Molecular Ionization For a Class of Diatomics in Intense Femtosecond Laser Fields, Phys. Rev. Lett. **85**, 2280 (2000).

[20] O. I. Tolstikhin, T. Morishita, and L. B. Madsen, Theory of tunneling ionization of molecules: Weak-field asymptotics including dipole effects, Phys. Rev. A **84**, 053423 (2011).

[21] L. B. Madsen, O. I. Tolstikhin, and T. Morishita, Application of the weak-field asymptotic theory to the analysis of tunneling ionization of linear molecules, Phys. Rev. A **85**, 053404 (2012).

[22] V. H. Trinh, O. I. Tolstikhin, L. B. Madsen, and T. Morishita, First-order correction terms in the weak-field asymptotic theory of tunneling ionization, Phys. Rev. A **87**, 043426 (2013).

[23] T. Endo, H. Fujise, H. Hasegawa, A. Matsuda, M. Fushitani, O. I. Tolstikhin, T. Morishita, and A. Hishikawa, Angle dependence of dissociative tunneling ionization of no in asymmetric two-color intense laser fields, Phys. Rev. A **100**, 053422 (2019).

[24] M. Okunishi, Y. Ito, V. Sharma, S. Aktar, K. Ueda, R. R. Lucchese, A. I. Dnestryan, O. I. Tolstikhin, S. Inoue, H. Matsui, and T. Morishita, Rescattering photoelectron spectroscopy of the CO_2 molecule: Progress towards experimental discrimination between theoretical target-structure models, Phys. Rev. A **100**, 053404 (2019).

[25] H. Fujise, M. Uemura, H. Hasegawa, D. Ikeya, A. Matsuda, T. Morishita, L. B. Madsen, F. Jensen, O. I. Tolstikhin, and A. Hishikawa, Helicity-dependent dissociative tunneling ionization of CF_4 in multicycle circularly polarized intense laser fields, Phys. Chem. Chem. Phys. **24**, 8962 (2022).

[26] O. I. Tolstikhin, L. B. Madsen, and T. Morishita, Weak-field asymptotic theory of tunneling ionization in many-electron atomic and molecular systems, Phys. Rev. A **89**, 013421 (2014).

[27] J. Kobus, L. Laaksonen, and D. Sundholm, A numerical Hartree-Fock program for diatomic molecules, Comput. Phys. Commun. **98**, 346 (1996).

[28] A. I. Dnestryan and O. I. Tolstikhin, Integral-equation approach to the weak-field asymptotic theory of

tunneling ionization, Phys. Rev. A **93**, 033412 (2016).

[29] A. I. Dnestryan, O. I. Tolstikhin, L. B. Madsen, and F. Jensen, Structure factors for tunneling ionization rates of molecules: General grid-based methodology and convergence studies, J. Chem. Phys. **149**, 164107 (2018).

[30] I. S. Wahyutama, D. D. Jayasinghe, F. Mauger, K. Lopata, M. B. Gaarde, and K. J. Schafer, An all-electron method for tunneling ionization of general molecules based on the weak-field asymptotic theory within the integral formulation (unpublished).

[31] L. B. Madsen, F. Jensen, O. I. Tolstikhin, and T. Morishita, Structure factors for tunneling ionization rates of molecules, Phys. Rev. A **87**, 013406 (2013).

[32] R. Saito, O. I. Tolstikhin, L. B. Madsen, and T. Morishita, Structure factors for tunneling ionization rates of diatomic molecules, At. Data Nucl. Data Tables **103-104**, 4 (2015).

[33] M. Valiev, E. Bylaska, N. Govind, K. Kowalski, T. Straatsma, H. Van Dam, D. Wang, J. Nieplocha, E. Apra, T. Windus, and W. de Jong, NWChem: A comprehensive and scalable open-source solution for large scale molecular simulations, Comput. Phys. Commun. **181**, 1477 (2010).

[34] P. Sándor, A. Sissay, F. Mauger, P. M. Abanador, T. T. Gorman, T. D. Scarborough, M. B. Gaarde, K. Lopata, K. J. Schafer, and R. R. Jones, Angle dependence of strong-field single and double ionization of carbonyl sulfide, Phys. Rev. A **98**, 043425 (2018).

[35] K. Lopata and N. Govind, Modeling fast electron dynamics with real-time time-dependent density functional theory: Application to small molecules and chromophores, J. Chem. Theory Comput. **7**, 1344 (2011).

[36] K. A. Hamer, F. Mauger, A. S. Folorunso, K. Lopata, R. R. Jones, L. F. DiMauro, K. J. Schafer, and M. B. Gaarde, Characterizing particle-like charge-migration dynamics with high-order harmonic sideband spectroscopy, Phys. Rev. A **106**, 013103 (2022).

[37] A. S. Folorunso, F. Mauger, K. A. Hamer, D. D. Jayasinghe, I. Wahyutama, J. R. Ragains, R. R. Jones, L. F. DiMauro, M. B. Gaarde, K. J. Schafer, and K. Lopata, Attochemistry regulation of charge migration, arXiv:2207.05892.

[38] A. Sissay, P. Abanador, F. Mauger, M. Gaarde, K. J. Schafer, and K. Lopata, Angle-dependent strong-field molecular ionization rates with tuned range-separated time-dependent density functional theory, J. Chem. Phys. **145**, 094105 (2016).

[39] P. Sándor, A. Sissay, F. Mauger, M. W. Gordon, T. T. Gorman, T. D. Scarborough, M. B. Gaarde, K. Lopata, K. J. Schafer, and R. R. Jones, Angle-dependent strong-field ionization of halomethanes, J. Chem. Phys. **151**, 194308 (2019).

[40] A. W. Lange, M. A. Rohrdanz, and J. M. Herbert, Charge-transfer excited states in a π-stacked adenine dimer, as predicted using long-range-corrected time-dependent density functional theory, J. Phys. Chem. B **112**, 6304 (2008).

[41] P. Krause, J. A. Sonk, and H. B. Schlegel, Strong field ionization rates simulated with time-dependent configuration interaction and an absorbing potential, J. Chem. Phys. **140**, 174113 (2014).

[42] L. J. Slater, *Handbook of Mathematical Functions with Formulas, Graphs, and Mathematical Tables*, edited by M. Abramowitz and I. A. Stegun (U.S. Dept. of Commerce, New York, 1972), Chap. 13.

[43] H. Li, D. Ray, S. De, I. Znakovskaya, W. Cao, G. Laurent, Z. Wang, M. F. Kling, A. T. Le, and C. L. Cocke, Orientation dependence of the ionization of CO and NO in an intense femtosecond two-color laser field, Phys. Rev. A **84**, 043429 (2011).

[44] R. Johansen, K. G. Bay, L. Christensen, J. Thøgersen, D. Dimitrovski, L. B. Madsen, and H. Stapelfeldt, Alignment-dependent strong-field ionization yields of carbonyl sulfide molecules induced by mid-infrared laser pulses, J. Phys. B: At. Mol. Opt. Phys. **49**, 205601 (2016).

[45] J. L. Hansen, L. Holmegaard, J. H. Nielsen, H. Stapelfeldt, D. Dimitrovski, and L. B. Madsen, Orientation-dependent ionization yields from strong-field ionization of fixed-in-space linear and asymmetric top molecules, J. Phys. B: At. Mol. Opt. Phys. **45**, 015101 (2012).

[46] D. Dimitrovski, M. Abu-samha, L. B. Madsen, F. Filsinger, G. Meijer, J. Küpper, L. Holmegaard, L. Kalhøj, J. H. Nielsen, and H. Stapelfeldt, Ionization of oriented carbonyl sulfide molecules by intense circularly polarized laser pulses, Phys. Rev. A **83**, 023405 (2011).

[47] H. Ohmura, N. Saito, and T. Morishita, Molecular tunneling ionization of the carbonyl sulfide molecule by double-frequency phase-controlled laser fields, Phys. Rev. A **89**, 013405 (2014).

[48] M. Abu-samha and L. B. Madsen, Effect of multielectron polarization in the strong-field ionization of the oriented CO molecule, Phys. Rev. A **101**, 013433 (2020).

[49] M. Abu-samha and L. B. Madsen, Multielectron effects in strong-field ionization of the oriented OCS molecule, Phys. Rev. A **102**, 063111 (2020).

[50] V. H. Trinh, O. I. Tolstikhin, and T. Morishita, First-order correction terms in the weak-field asymptotic theory of tunneling ionization in many-electron systems, J. Phys. B: At. Mol. Opt. Phys. **49**, 195603 (2016).

[51] P. Hoerner and H. B. Schlegel, Angular dependence of strong field ionization of CH_3X (X = F, Cl, Br, or I) using time-dependent configuration interaction with an absorbing potential, J. Phys. Chem. A **121**, 5940 (2017).

[52] See http://www.hpc.lsu.edu.

[53] See http://www.loni.org.